

Analysis of the interchannel response in a MEMS $1 \times N^2$ wavelength-selective switch

Jui-che Tsai,^{1,*} Chun-Yi Yin,¹ Chia-Wei Sun,² and Ming C. Wu³

¹Graduate Institute of Electro-Optical Engineering and Department of Electrical Engineering,
National Taiwan University, Taipei, Taiwan

²Medical Electronics and Device Technology Center, Industrial Technology Research Institute, Hsinchu, Taiwan

³University of California, Berkeley, Department of Electrical Engineering and Computer Sciences and Berkeley Sensor and Actuator Center (BSAC), Berkeley, California 94720-1774, USA

*Corresponding author: jctsay@cc.ee.ntu.edu.tw

Received 19 June 2006; revised 24 November 2006; accepted 6 February 2007;
posted 6 February 2007 (Doc. ID 72106); published 15 May 2007

A theoretical model based on Fourier optics and the power-coupling overlap integral is built to investigate the interchannel response in a micro-electro-mechanical systems $1 \times N^2$ wavelength-selective switch. The simulation results demonstrate that the interchannel response depends significantly on the output port location and the radius of curvature of the micromirrors. For the output originally aligned with the input along the dispersion direction, it is possible to achieve interchannel-response suppression by rotating the two-dimensional (2D) collimator array by a slight angle, e.g., 20° . Experimental results under different conditions are also shown. © 2007 Optical Society of America

OCIS codes: 060.1810, 060.4510, 230.4040, 230.3990.

1. Introduction

Dynamic wavelength-selective switches (WSSs) have been of great interest as they integrate wavelength demultiplexing, switching, and remultiplexing functions in compact packages [1–12]. They also enable management of optical networks at the wavelength level and are the building blocks of wavelength-selective crossconnects (WSXC) [1]. A wavelength-selective switch can be realized by various distinct techniques, such as the free-space MEMS (micro-electro-mechanical systems) optical system with a tilting-micromirror array [1–8], the hybrid PLC (planar lightwave circuit)-MEMS architecture [9–11], and liquid crystal-based modules [12].

The ancestor of nowadays free-space MEMS WSSs is the MEMS dynamic add-drop multiplexer reported by Ford *et al.* [13]. It is essentially a 1×2 WSS. Until now, the maximum output port count for a free-space MEMS $1 \times N$ WSS with a one-dimensional (1D) collimator array is $N = 4$ [1–3]. The port count can be increased from N to N^2 by using

a two-dimensional (2D) collimator array in conjunction with a two-axis beam-steering mechanism [4–8]. The two-axis beam steering is implemented by either two linear arrays of one-axis analog micromirrors with orthogonal scanning directions [4], or a monolithic two-axis MEMS scanner array [5–8].

The hybrid PLC-MEMS approach was used by Metconnex to commercially implement a 1×9 WSS [10,11]. Two PLC chips, each with five input/output ports, were stacked vertically. This architecture is analogous to the free-space MEMS $1 \times N^2$ WSS and also requires a two-axis micromirror array. The same company also offers 1×14 and 1×24 modules [11]. A liquid crystal-based WSS, manufactured by CoAdna Photonics, is available with a nominal output port count of 8. It can be extended to 1×9 , 1×10 , or more ports [12].

In our previous study of free-space MEMS $1 \times N^2$ WSSs, we observed a large interchannel response at a horizontal output port that is aligned with the input along the dispersion direction [4]. Similar phenomena have also been discovered in MEMS-based channeled dynamic spectral equalizers with the micromirrors tilting in the dispersion direction [14,15].

The interchannel response is undoubtedly undesirable for optical communication. It is preferable to suppress the interchannel response, therefore maximizing the pass and stop bandwidths, allowing for channel misalignment due to laser drift from the ITU grid, and relaxing packaging requirements. We present a theoretical model based on Fourier optics and the power-coupling overlap integral. The interchannel response in a MEMS $1 \times N^2$ WSS is investigated and it, according to the simulation results, depends significantly on the output port location and the radius of curvature of the micromirrors. A simple solution is then proposed to suppress the interchannel response in a $1 \times N^2$ WSS. It can be achieved by rotating the 2D collimator array such that no output port is aligned with the input along the dispersion direction [5]. With 20° rotation, 10 and 8.2 dB suppressions are demonstrated theoretically and experimentally, respectively, for a prototype system.

2. Theoretical Model

Figure 1 shows the schematic of the $1 \times N^2$ WSS. The 2D collimator array is mounted on a rotary stage with rotation axis parallel to the optical beams. The center collimator serves as the input port. The WDM signals are spatially dispersed by the grating and focused onto their corresponding mirrors by the resolution lens. The two-axis mirrors direct individual wavelengths to the desired output ports. The telescope beam expander reduces the optical spot size on the MEMS mirror.

The simulation model can be explained with the assistance of Fig. 2. For simplicity, the telescope beam expander and the grating are neglected. The field distribution E_{input} emerging from the input fiber collimator contains both amplitude and phase information. It is projected by the resolution lens to the back focal plane, where the MEMS mirror array is situated. The projected field, denoted by e_{input} , is then spatially modulated by the micromirrors, resulting in a modulated field distribution e_{input}' at the back focal plane. e_{input}' yields a projected field E_{input}' at the front focal plane, where the collimators are located. The power-coupling efficiency into a specific output fiber collimator is then $\eta = |\iint E_{input}' \cdot E_{output}^* dx dy|^2$,

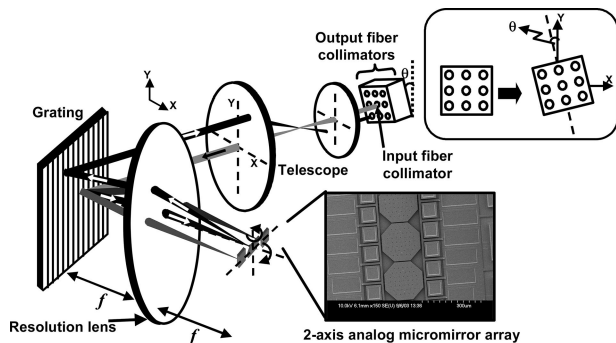


Fig. 1. Schematic of the $1 \times N^2$ WSS with a rotated 2D collimator array. A two-axis analog micromirror array is used for 2D beam steering. The telescope expands the size of the optical beam.

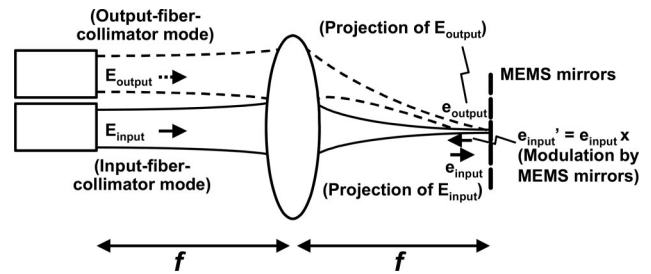


Fig. 2. Illustration of the theoretical model based on Fourier optics.

where E_{output} is the modal field distribution of the output collimator [16]. Note that all the field distributions mentioned above are with normalized power, and E_{output} is identical to E_{input} except for a shift in space if all the collimators are identical. Based on Fourier optics [17], E_{input}' and E_{output} are the Fourier transforms of e_{input}' and e_{output} , respectively, where e_{output} is the projected field of the output collimator onto the MEMS device plane (i.e. the back focal plane). According to the properties of the Fourier transform, $|\iint E_{input}' \cdot E_{output}^* dx dy|^2 = |\iint e_{input}' \cdot e_{output}^* dx dy|^2$. Therefore, the power-coupling efficiency can be obtained by calculating the overlap integral $|\iint e_{input}' \cdot e_{output}^* dx dy|^2$, which normally has a much simpler form.

The normalized field distribution e_{output} , the projected image of the output collimator on the MEMS device plane, has a Gaussian shape and is given by

$$e_{output}(x, y, f) = \left(\frac{2}{\pi \omega_{0x} \omega_{0y}} \right)^{1/2} \exp \left[- \frac{\left(x - \frac{pf}{f_0} \right)^2}{\omega_{0x}^2} - \frac{y^2}{\omega_{0y}^2} \right] \times \exp[jkx \sin \theta_x + jky \sin \theta_y]. \quad (1)$$

The parameters used for our simulation are the same as those in the experiment. ω_{0x} and ω_{0y} are the Gaussian beam radii in the x and y directions, respectively. The beam radius emerging from the collimator array is originally $125 \mu\text{m}$. It is then expanded to 2 mm after passing through the telescope. This leads to a focused spot on the device plane with ω_{0x} and ω_{0y} being $69 \mu\text{m}$ and $76 \mu\text{m}$, respectively. ω_{0x} and ω_{0y} have different quantities due to the anamorphic effect caused by the diffraction grating. The MEMS mirror pitch (i.e. center-to-center distance between adjacent mirrors), p , is $200 \mu\text{m}$, while the channel spacing f_0 is 125 GHz . The spatial dispersion resulting from the diffraction grating is explicitly expressed. The term pf/f_0 determines the center location of the Gaussian mode, which is a function of the frequency shift f . The output fiber collimator is located laterally off the optical axis of the system, resulting in a phase distribution in the projected field e_{output} and therefore the term $\exp[jkx \sin \theta_x + jky \sin \theta_y]$. Given the exact location of the output port, θ_x and θ_y can be calculated by either ray tracing or the shift theorem of the Fourier transform.

The field distribution e_{output} , the modulated field by the MEMS mirror array, is given by [15]

$$e_{\text{input}}(x, y, f) = \left(\frac{2}{\pi \omega_{0x} \omega_{0y}} \right)^{1/2} \exp \left[-\frac{\left(x - \frac{pf}{f_0} \right)^2}{\omega_{0x}^2} - \frac{y^2}{\omega_{0y}^2} \right] \times \sum_{\zeta=0}^{N-1} A_{\zeta} \exp[jk[x - \zeta p] \sin \theta_{x\zeta} + jky \sin \theta_{y\zeta} + \phi_{\zeta}] \text{rect} \left[\frac{x - \zeta p}{p - \text{gap}} \right]. \quad (2)$$

N represents the total number of MEMS mirrors while $\theta_{x\zeta}$ and $\theta_{y\zeta}$ are twice the tilt angles of the ζ^{th} mirror in the x and y directions, respectively. The amplitude attenuation coefficient A_{ζ} is set to be 1, assuming a perfect mirror surface with 100% reflection. The constant phase ϕ_{ζ} accounts for the mirror sagging. It is set to be 0 in the simulation, assuming a sag-free mirror array.

In our simulation, the mirror of $\zeta = 1$ in the array is tilted such that the corresponding wavelength channel is switched to the targeted output fiber collimator. The values of θ_{x1} and θ_{y1} are then determined by the output port coordinate, which varies while rotating the fiber collimator array. For other mirrors without tilt, both $\theta_{x\zeta}$ and $\theta_{y\zeta}$ are 0, implying that the corresponding channels are coupled back to the input port.

The rectangular function results from the finite extent of each mirror. The gap between mirrors has also been taken into account. In our simulation and experiment, mirrors with an octagonal shape are also of interest. It is not as straightforward to have an explicit expression for the octagonal shape embedded in Eq. (2). However, its effect on the coupling efficiency can be addressed by manipulating the integration interval of $\eta = \left| \iint e_{\text{input}}' \cdot e_{\text{output}}^* dx dy \right|^2$, in which the interval of integration is defined by the mirror areas.

In Eq. (2) the effect of mirror curvature has not been included. If the mirror curvature is to be considered, an additional phase term of

$$\exp \left[jk \frac{(x - \zeta p)^2 + y^2}{R} \right]$$

should be incorporated for each mirror, where R is the radius of curvature of the mirror.

3. Simulation Results

For a selected output that is aligned with the input along the horizontal direction (i.e. dispersion direction), the projected image of the output collimator possesses a phase variation along the MEMS mirror array. The gap, which is equivalent to a dark zone between mirrors, leads to a phase jump for any interchannel wavelength whose field distribution crosses two adjacent mirror pixels. While calculating the coupling efficiency, this results in a nonvanishing

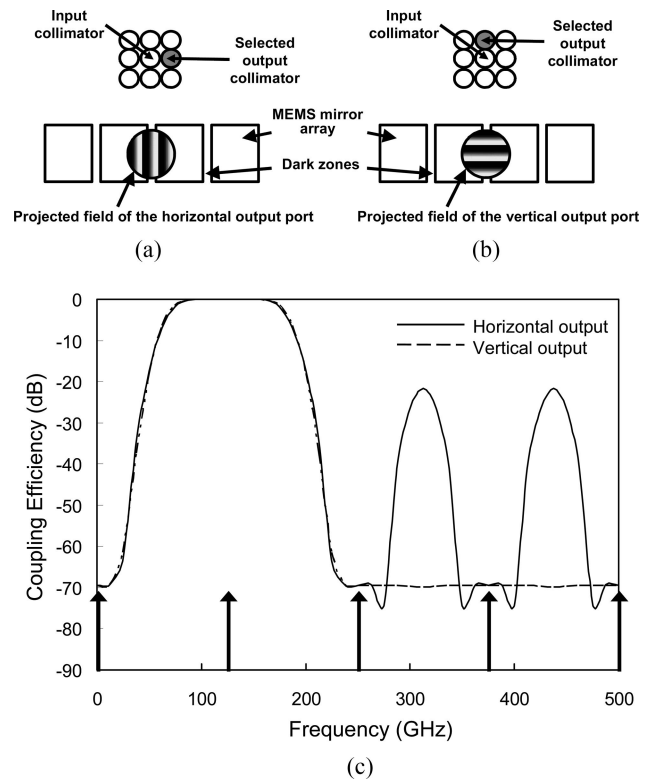


Fig. 3. Phase variations of the projected images of (a) a horizontal output port and (b) a vertical output port. The simulation results are shown in (c).

overlap integral even if the mirrors are not tilted. On the other hand, if the output is aligned with the input along the vertical direction (i.e. direction orthogonal to dispersion), the projected image of the output then experiences a phase variation along the direction perpendicular to the MEMS mirror array. In this case, the gap introduces no phase jump for the interchannel wavelengths and hence no interchannel response is observed. The above comparison is shown in Fig. 3. The simulated output spectra [Fig. 3(c)] are obtained with perfectly flat rectangular mirrors. The mirror of $\zeta = 1$ is tilted to switch the corresponding channel, $f = 125$ GHz. For simplicity, the anamorphic effect arising from the grating has been neglected and the radii of the projected image on the MEMS device plane are set to be $\omega_{0x} = \omega_{0y} = 38 \mu\text{m}$, different from those used for the experiment and the following simulation ($\omega_{0x} = 69 \mu\text{m}$, $\omega_{0y} = 76 \mu\text{m}$).

In our experiment, MEMS mirrors with curvature and an octagonal shape are used. Therefore, the following simulation calculates the power-coupling efficiency versus frequency shift using such mirror conditions. We consider two different mirror curvatures, $R = 30$ mm and $R = 10$ mm. For each curvature, the output spectra under three rotation angles of the collimator array, 0° , 10° , and 20° , are simulated. With 0° rotation, the selected output is aligned with input along the horizontal direction. Figure 4(a) demonstrates the simulation results for $R = 30$ mm.

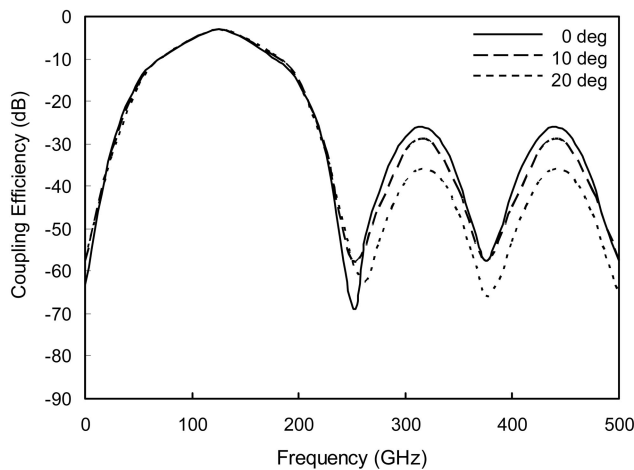
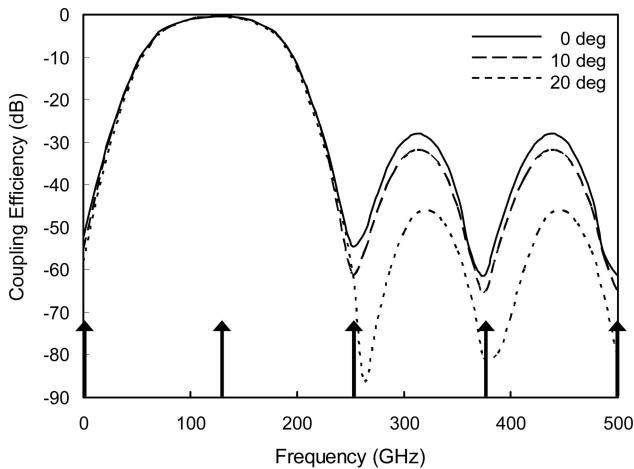


Fig. 4. Simulation results for (a) $R = 30$ mm and (b) $R = 10$ mm. Output spectra for each curvature are simulated with 0° , 10° , and 20° rotations of the collimator array. The arrows indicate the channel centers.

The arrows indicate the channel centers. When there is no rotation of the collimator array (0°), a pronounced interchannel response at -27.4 dB below the signal ($f = 125$ GHz) is exhibited. The interchannel response is reduced to -31.3 dB (3.9-dB suppression) and -46.3 dB (18.9-dB suppression) below the signal for 10° and 20° rotations, respectively. The results for $R = 10$ mm are shown in Fig. 4(b). When the collimator array is not rotated (0°), an interchannel response at -23 dB below the signal is observed. Compared with the case of $R = 30$ mm, the signal level is decreased to -3.1 dB due to a larger mirror curvature. The interchannel response is suppressed to -26.0 dB (3-dB suppression) and -33 dB (10-dB suppression) below the signal for 10° and 20° rotations, respectively.

The dispersion characteristic in a free-space MEMS WSS is also of interest. Previously, Neilson *et al.* investigated the relation between the dispersion and the micromirror curvature in a MEMS-based channeled dispersion compensator [18]. The curva-

ture resulted in a wavelength-dependent path-length difference, and therefore dispersion within the passband. Their derivation was under Littrow configuration and can be further modified for our case, in which the incident and diffracted beams of the grating meet at a small angle. The wavelength-dependent path-length difference $\Delta z(\Delta\lambda)$, relative to the center wavelength λ_0 of the passband, can then be expressed as follows:

$$\Delta z(\Delta\lambda) = \left(\frac{4f^2 \tan^2 \theta_r}{R\lambda_0} \Delta\lambda \right) \left(1 + \left| \frac{\sin \theta_i}{\sin \theta_r} \right| \right), \quad (3)$$

where f is the focal length of the resolution lens while $\Delta\lambda$ is the offset from the center wavelength λ_0 . θ_i and θ_r are the incident and diffracted angles on the grating, respectively. The group delay within the passband (corresponding mirror: $\zeta = 1$) of Fig. 4 is plotted in Fig. 5 for both mirror curvatures. The center wavelength is set to be 1551 nm, while f , θ_i , and θ_r are 30 cm, 33° , and -22.6° , respectively. The dispersion

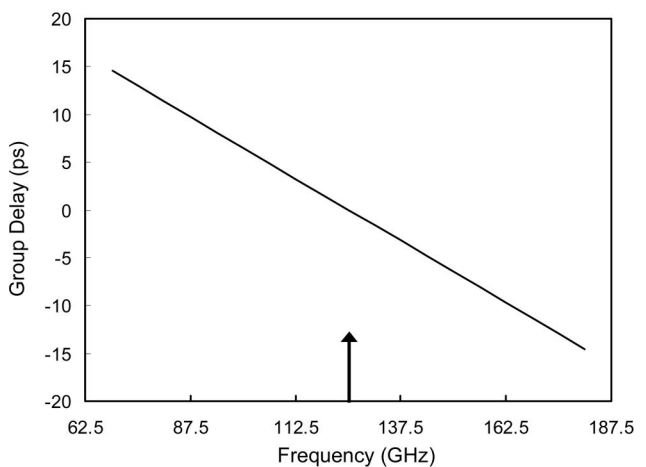
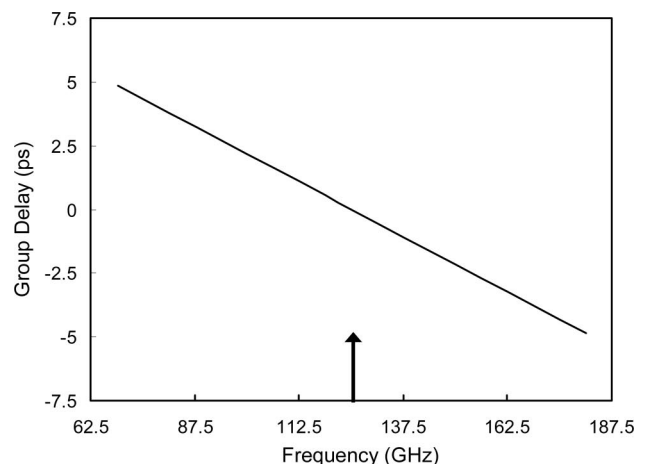


Fig. 5. Relative group delay within the passband of Fig. 4 for (a) $R = 30$ mm and (b) $R = 10$ mm.

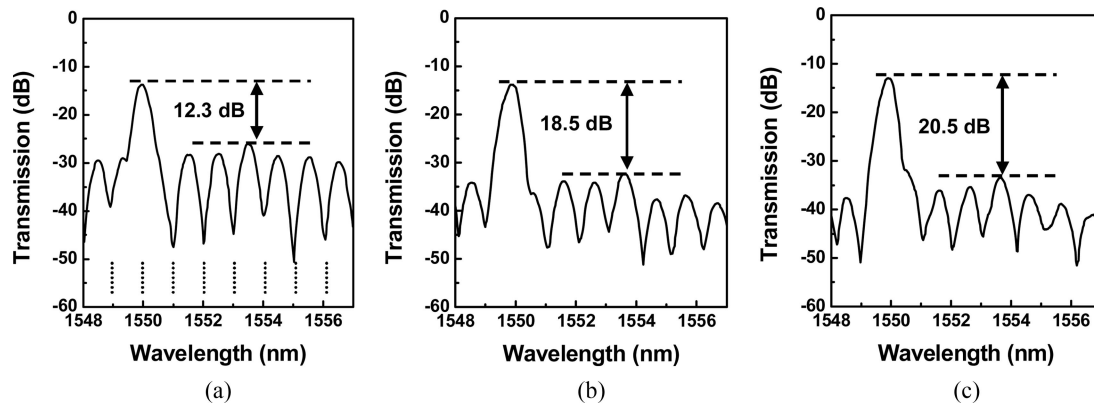


Fig. 6. Optical spectra from a selected output port which is horizontally aligned with the input at 0° rotation, when the collimator array is rotated by (a) 0° , (b) 10° , and (c) 20° . The dotted lines in (a) indicate the positions of the wavelength channels. The minor peaks between dotted lines are the interchannel response.

is 11 ps/nm for $R = 30$ mm and 32 ps/nm for $R = 10$ mm.

It can be seen that the mirror flatness plays an important role and the larger curvature of $R = 10$ mm has reduced the interchannel-response suppression, especially for 20° rotation. Greater curvature also increases the dispersion within the passband. For a perfectly flat ($R = \infty$) rectangular mirror, the interchannel response is calculated to be -26.9 dB, -35.1 dB (8.2-dB suppression), and -59.4 dB (32.5-dB suppression) below the signal for rotations of 0° , 10° , and 20° , respectively.

Most WSSs have the ability to attenuate signals. In the free-space micromirror-based module, it is done by tuning the mirror angles. For simplicity, we simulate the attenuation functionality using the same parameters as those of Fig. 3. It is found that the interchannel response varies with the attenuation level. For 0° rotation of the 2D collimator array, the interchannel response between two pass channels with 20-dB attenuation is 5 dB above the attenuated passband signal. When the passband attenuation is increased to 40 dB, the interchannel response becomes 28 dB above.

4. Experimental Results

A 1×10 two-axis micromirror array with 200- μm pitch and 98% fill factor is used in the experiment [5], as shown in the inset of Fig. 1. The mirrors have radii of curvature within the range of 10 ± 2 mm. The mechanical scan angles are $\pm 2.63^\circ$ (at 14.1V) and $\pm 1.27^\circ$ (at 21.1V) for rotation about y and x axes, respectively. The MEMS devices are fabricated using the SUMMiT-V surface micromachining process provided by Sandia National Laboratory. In this prototype system, a 600-grooves/mm grating is used. The focal length of the resolution lens is 30 cm. The channel spacing is 125 GHz. It can be adjusted to comply with the telecommunication-required 50 or 100 GHz spacing by using an 1100 grooves/mm grating, which provides greater dispersion strength and is more commonly used in free-space WDM systems. A commercial 6×6 collimator array with a 1 mm pitch and

a 125 μm beam radius (ω_0) is employed in our system. A $16\times$ telescope expands the optical beams. The collimator array is rotated by small angles (10° , 20°) to mitigate the interchannel response. Figure 6 shows the spectra from the selected output port at three different rotation angles (0° , 10° , and 20°). The measurement resolution is limited by the optical spectrum analyzer available in our laboratory, whose finest resolution bandwidth is 0.08 nm. At 0° , the input and output ports are aligned in the dispersion direction. The dotted lines in Fig. 5(a) indicate the positions of channel centers for this WSS. The 1550-nm wavelength is switched to this output port. Signals at other wavelength channels are below ~ -35 dB. However, the response between channels (between dotted lines) are very pronounced (-12.3 dB below the signal). The interchannel response is reduced to -18.5 dB (6.2-dB suppression) and -20.5 dB (8.2-dB suppression) below the signal at 10° and 20° , respectively. The power level of the OFF channels is higher than those obtained in the simulation as it is eventually clamped by the noise floor of the experiment. The relatively high insertion loss and the suppression deviation from simulation may be due to optical system misalignment, excess mirror curvature, or mirror sagging. With the radius of curvature within the range of 10 ± 2 mm, the dispersion falls between 27 ps/nm and 41 ps/nm.

5. Conclusions

The interchannel response of a $1 \times N^2$ wavelength-selective switch (WSS) with a two-axis micromirror array has been successfully studied theoretically and experimentally. The simulation results show that the interchannel response depends strongly on the output port location as well as the MEMS mirror curvature. With 20° rotation of the 2D collimator array, 10 and 8.2 dB suppressions are demonstrated theoretically and experimentally, respectively, for a prototype system. Greater suppression of up to 32.5 dB at 20° rotation is expected with perfectly flat rectangular micromirrors.

This work was supported by DARPA/SPAWAR under contract N66001-00-C-8088, National Science Council of Taiwan under grants NSC 94-2218-E-002-082 and NSC 95-2221-E-002-053, and Excellent Research Projects of National Taiwan University, 95R0062-AE00-06.

References

1. T. Ducellier, J. Bismuth, S. F. Roux, A. Gillet, C. Merchant, M. Miller, M. Mala, Y. Ma, L. Tay, J. Sibille, M. Alavanja, A. Deren, M. Cugalj, D. Ivancevic, V. Dhuler, E. Hill, A. Cowen, B. Shen, and R. Wood, "The MWS 1×4 : a high performance wavelength switching building block," in *ECOC 2002, 28th European Conference on Optical Communication* (IEEE, 2002), paper 2.3.1.
2. J. C. Tsai, S. Huang, D. Hah, H. Toshiyoshi, and M. C. Wu, "Open-loop operation of MEMS-based $1 \times N$ wavelength-selective switch with long-term stability and repeatability," *IEEE Photon. Technol. Lett.* **16**, 1041–1043 (2004).
3. D. M. Marom, D. T. Neilson, D. S. Greywall, C. S. Pai, N. R. Basavanahally, V. A. Aksyuk, D. O. López, F. Pardo, M. E. Simon, Y. Low, P. Kolodner, and C. A. Bolle, "Wavelength-selective $1 \times K$ switches using free-space optics and MEMS micromirrors: theory, design, and implementation," *J. Lightwave Technol.* **23**, 1620–1630 (2005).
4. J. C. Tsai, S. Huang, D. Hah, and M. C. Wu, " $1 \times N^2$ wavelength-selective switch with two cross-scanning one-axis analog micromirror arrays in a $4-f$ optical system," *J. Lightwave Technol.* **24**, 897–903 (2006).
5. J. C. Tsai and M. C. Wu, " $1 \times N^2$ wavelength-selective switches with tilted 2D collimator arrays for inter-channel-response suppression," in *Conference on Lasers and Electro-Optics, 2004 OSA Technical Digest Series* (Optical Society of America, 2004), paper CTuFF7.
6. J. C. Tsai and M. C. Wu, "Gimbal-less MEMS two-axis optical scanner array with high fill-factor," *J. Microelectromech. Syst.* **14**, 1323–1328 (2005).
7. J. C. Tsai and M. C. Wu, "Design, fabrication, and characterization of a high fill-factor, large scan-angle, two-axis scanner array driven by a leverage mechanism," *J. Microelectromech. Syst.* **15**, 1209–1213 (2006).
8. J. C. Tsai and M. C. Wu, "A high port-count wavelength-selective switch using a large scan-angle, high fill-factor, two-axis MEMS scanner array," *IEEE Photon. Technol. Lett.* **18**, 1439–1441 (2006).
9. D. M. Marom, C. R. Doerr, N. R. Basavanahally, M. Cappuzzo, L. Gomez, E. Chen, A. Wong-Foy, and E. Laskowski, "Wavelength-selective 1×2 switch utilizing a planar lightwave circuit stack and a MEMS micromirror array," in *Proceedings of 2004 IEEE/LEOS International Conference on Optical MEMS and Their Applications* (IEEE, 2004), pp. 28–29.
10. T. Ducellier, A. Hnatiw, M. Mala, S. Shaw, A. Mank, D. Touahri, D. McMullin, T. Zami, B. Lavigne, P. Peloso, and O. Leclerc, "Novel high performance hybrid waveguide-MEMS 1×9 wavelength selective switch in a 32-cascade loop experiment," in *ECOC 2004, European Conference on Optical Communication* (IEEE, 2004), paper Th4.2.2.
11. http://www.lightreading.com/document.asp?doc_id=69809&site=ofc.
12. http://www.coadna.com/CoAdna_1x8_2-28-06.pdf.
13. J. E. Ford, V. A. Aksyuk, D. J. Bishop, and J. A. Walker, "Wavelength add-drop switching using tilting micromirrors," *J. Lightwave Technol.* **17**, 904–911 (1999).
14. D. M. Marom and S.-H. Oh, "Filter-shape dependence on attenuation mechanism in channelized dynamic spectral equalizers," in *Proceedings of the Fifteenth Annual Meeting of the IEEE Lasers and Electro-Optics Society* (IEEE, 2002), Vol. 2, pp. 416–417.
15. S. H. Oh and D. M. Marom, "Attenuation mechanism effect on filter shape in channelized dynamic spectral equalizers," *Appl. Opt.* **43**, 127–131 (2004).
16. R. E. Wagner and W. J. Tomlinson, "Coupling efficiency of optics in single-mode fiber components," *Appl. Opt.* **21**, 2671–2688 (1982).
17. J. W. Goodman, *Introduction to Fourier Optics* (McGraw-Hill, 1996).
18. D. T. Neilson, R. Ryf, F. Pardo, V. A. Aksyuk, M.-E. Simon, D. O. Lopez, D. M. Marom, and S. Chandrasekhar, "MEMS-based channelized dispersion compensator with flat passbands," *J. Lightwave Technol.* **22**, 101–105 (2004).